

Bayesian inferences on covariant density functionals from multimessenger astrophysical data: The impacts of likelihood functions of low density matter constraints

Jia-Jie Li^{1,*} and Armen Sedrakian^{2,3,†}

¹*School of Physical Science and Technology, Southwest University, Chongqing 400715, China*

²*Frankfurt Institute for Advanced Studies, D-60438 Frankfurt am Main, Germany*

³*Institute of Theoretical Physics, University of Wrocław, 50-204 Wrocław, Poland*

(Dated: May 5, 2025)

We systematically investigate how the choice between Gaussian and uniform likelihood functions in Bayesian inference affects the inferred bulk properties of compact stars and nuclear matter within covariant density functional-based equations of state. To enable direct comparison between two approaches, we designed the uniform likelihood function with a Gaussian-equivalent normalization factor and marginalization behavior. Across three representative astrophysical scenarios, both approaches yield nearly identical mass-radius relations, density-pressure relations, and overlapping 95.4% confidence level regions. We find significant variations in the predicted distributions of nuclear characteristics at nuclear saturation in the isoscalar channel, e.g., in nuclear compressibility K_{sat} , whereas the isovector quantities, for example, proton fraction, are quite similar. Our results indicate that the influence of individual nuclear characteristics at saturation density on the global properties of compact stars is obscured by the integral nature of these quantities. This, in turn, underscores the need for dedicated nuclear experiments sensitive to these characteristics in order to better constrain their values.

I. INTRODUCTION

Understanding the physics of nuclear matter over a wide range of densities and isospin asymmetries is essential for the description of the behavior of neutron-rich nuclei, heavy-ion reactions, the structure of compact stars (CSs), and related problems. In particular, the equation of state (EOS) of nuclear matter can be derived from modeling the physics of these systems within different approaches, ranging from density functional methods to microscopic *ab initio* calculations. In the process of discerning the valid set of EoS, the statistical inference of its parameters from the data, including multimessenger astrophysics, is of crucial importance.

The Bayesian inference framework, involving various theoretical and observational constraints, has been applied to EOS models covering the *ab initio* calculations combining model-agnostic extrapolations such as the use of polytropes or speed-of-sound schemes [1–11], the meta-type models parametrized by nuclear characteristic parameters [12–15], the non-relativistic models based on effective nuclear potentials like the Skyrme interactions [15–19], and the covariant density functional (CDF) based models [20–35].

The CDF models are commonly separated into two broad classes: those with non-linear meson contributions to the effective Lagrangian, and those that maintain only linear coupling but incorporate density-dependent couplings to account for medium modifications of meson-nucleon vertices. Both approaches offer flexibility, the first class through various self- and cross-couplings between mesons, and the second class through different forms of density-dependence. This adaptability allows one to tailor the models to address specific physics questions, see Refs. [36–40] for reviews. In a CDF-based Bayesian analysis, current knowledge of the isospin-

asymmetric EOS near saturation density is typically encoded as constraints on the Taylor expansion coefficients of energy density of nuclear matter close to saturation density (ρ_{sat}) and the isospin symmetrical limit. Specifically, the incompressibility (K_{sat}) and symmetry energy slope (L_{sym}) parameters, determined from giant resonance experiments or nuclear collision data, provide important complementary constraints. The low-density region parameters can be further calibrated using microscopic computations, which are typically based on potentials derived from chiral effective field theory (χ EFT) calculations, which are suitable for describing nuclear and neutron matter at densities $\leq 2\rho_{\text{sat}}$ [41–44].

In addition to the various CDF models used in Bayesian analysis, different approaches exist for imposing low-density matter constraints from theory and measurements, including their uncertainties. The most common method involves variable likelihood functions, particularly Gaussian-type functions, which build a probabilistic model accounting for uncertainties in each constraint. An alternative approach is the Heaviside method, which makes no specific assumptions about uncertainty distributions but simply rejects EOS models outside defined lower and upper boundaries. Gaussian functions are typically used for implementing nuclear matter Taylor expansion coefficient constraints with preferred values, while the Heaviside method is more commonly applied for χ EFT constraints, see for example, Refs. [21, 22, 25–29, 31–35]. Recently, a third approach was proposed - a “uniform-Gaussian combination” method [31], where the 1σ domain of a Gaussian distribution is replaced by a uniform distribution, providing a hybrid framework for constraint implementation. This hybrid approach will be referred to as “uniform-Gaussian-combination”.

In the present work, we employ both Gaussian and uniform-Gaussian-combination likelihood functions to characterize low-density nuclear matter properties. In doing so, we maintain the same astrophysical constraints to study how different likelihood function choices impact Bayesian analysis predictions. This work is motivated by the observation that numer-

* jjli@swu.edu.cn

† sedrakian@fias.uni-frankfurt.de

ous analyses consistently constrain only the first few coefficients of the Taylor expansion of nuclear matter near ρ_{sat} to within 5% [12, 45–47]. This is not the case for the higher-order coefficients [12, 48].

For example, the incompressibility parameter K_{sat} has been determined from giant monopole resonance experiments to be $230 \pm 40 \text{ MeV}$ [47, 49–51]. Heavy-ion collision analyses yield results with larger uncertainties. Elliptic flow measurements compared with IQMD simulations suggest an incompressibility of $K_{\text{sat}} = 190 \pm 30 \text{ MeV}$ [52]. Proton directed and elliptic flow measurements compared with pBUU transport models indicate $K_{\text{sat}} = 210\text{--}300 \text{ MeV}$ [53]. Analyzing the Kaon yields experimental results together with RQMD and IQMD calculations enabled extraction of the EOS characterized by $K_{\text{sat}} = 200 \text{ MeV}$ [54, 55]. Comparison of FOPI data for rapidity-dependent elliptic flow with UrQMD simulations give $K_{\text{sat}} = 220 \pm 40 \text{ MeV}$ [56]. Recently, a Bayesian analysis of STAR flow data suggests a relatively hard equation of state with $K_{\text{sat}} = 285 \pm 67 \text{ MeV}$ [57]. This broad range of constraints on K_{sat} indicates that there is no consensus value yet. Similar challenges exist in constraining the symmetry energy slope parameter L_{sym} , see for example, Refs. [58–65]. Therefore, comparing inferences based on different likelihood functions allows us to test the consistency of various statistical approaches and ultimately establish tighter constraints on the EOS across the full relevant density range. By examining how different statistical treatments affect conclusions, we can better understand which constraints are most susceptible to the methodology, potentially leading to more reliable determinations of nuclear matter properties from low densities to the extreme densities found in CSs.

This paper is structured as follows. In Sec. II we introduce the specific EOS model employed in this work. In Sec. III we discuss the Bayesian inference framework and define the various likelihood functions adopted for various constraints. Our analysis of the impact of different choices of the likelihood functions on the predictions of the model is given in Sec. IV. Here we present the results of a comparison of gross properties of CSs and nucleonic matter. Our conclusions are given in Sec. V.

II. CDF FOR STELLAR MATTER

To ensure this presentation is self-contained, we briefly review the general feature of CDF approach, also given in the first two papers of these series [33, 35] and reviewed in Ref. [40]. We use the meson-exchange version with density dependent couplings. The Lagrangian of stellar matter with nucleonic degrees of freedom reads $\mathcal{L} = \mathcal{L}_N + \mathcal{L}_m + \mathcal{L}_l$, where the effective nucleonic Lagrangian is given by

$$\mathcal{L}_N = \sum_N \bar{\psi}_N \left[\gamma^\mu (i\partial_\mu - g_\omega \omega_\mu - g_\rho \boldsymbol{\tau} \cdot \boldsymbol{\rho}_\mu) - (m_N - g_\sigma \sigma) \right] \psi_N, \quad (1)$$

where ψ_N are the nucleonic Dirac fields with masses m_N , and σ , ω_μ , and ρ_μ are the mesonic fields that mediate the nuclear

TABLE I. The minimal (“min”) and maximal (“max”) values of the variation range of the CDF parameters over which uniform prior distributions have been assigned.

No.	Parameter	min	max
1	g_σ	7.5	12.5
2	g_ω	9.0	16.0
3	g_ρ	2.5	5.0
4	a_σ	0.8	2.2
5	d_σ	0.0	2.2
6	d_ω	0.0	2.2
7	a_ρ	0.0	1.5

interactions. The remaining pieces of the Lagrangian correspond to the mesonic and leptonic contributions, respectively. In practice, the masses of nucleons, mesons and leptons are fixed to be (or close to) the ones in the vacuum [35].

The meson-nucleon couplings depend on the vector nucleonic density $\rho = \langle \psi^\dagger \psi \rangle$, which were assumed as

$$g_m(\rho) = g_m(\rho_{\text{sat}}) f_m(r), \quad (2)$$

with a constant value $g_m(\rho_{\text{sat}})$ at saturation density ρ_{sat} , and a function $f_m(r)$ of the ratio $r = \rho/\rho_{\text{sat}}$. For the isoscalar channel, the density dependence is defined as [45, 46]

$$f_m(r) = a_m \frac{1 + b_m(r + d_m)^2}{1 + c_m(r + d_m)^2}, \quad m = \sigma, \omega, \quad (3)$$

with five conditions:

$$f_m(1) = 1, \quad f_m''(0) = 0, \quad f_\sigma''(1) = f_\omega''(1), \quad (4)$$

which reduce the number of adjustable parameters. For the isovector channel the density dependence is taken in an exponential form [45, 46]:

$$f_\rho(r) = \exp[-a_\rho(r - 1)]. \quad (5)$$

To describe cold, neutrino-free, and catalyzed stellar matter, we further require weak equilibrium and charge neutrality that prevail in CSs [40]. The EOS of stellar matter and the corresponding composition, then, can be computed uniquely in terms of seven adjustable parameters

$$\boldsymbol{\theta}_{\text{EOS}} = (g_\sigma, g_\omega, g_\rho, a_\sigma, d_\sigma, d_\omega, a_\rho), \quad (6)$$

that enter our Bayesian inference. These are the three coupling constant at nuclear saturation density ($g_\sigma, g_\omega, g_\rho$) and four parameters ($a_\sigma, d_\sigma, d_\omega, a_\rho$) that control their density dependences, for those we take uniform prior distributions with the intervals listed in Table I.

III. INFERENCE FRAMEWORK AND CONSTRAINTS

We perform a Bayesian analysis for CDF approach by applying nuclear and astrophysical constraints. The details of the techniques used can be found in Refs. [33, 35]. For the sake of completeness, we present here a few key aspects and highlight additional changes made for the likelihood functions.

A. Low density matter constraints and the likelihoods

The bulk properties of nuclear matter is customarily quantified in terms of the *nuclear matter characteristics at saturation density*, which are the coefficients of the expansion of the energy density close to the saturation density and isospin-symmetrical limits

$$E(\rho, \delta) \simeq E_{\text{sat}} + \frac{1}{2!} K_{\text{sat}} \chi^2 + \frac{1}{3!} Q_{\text{sat}} \chi^3 + \frac{1}{4!} Z_{\text{sat}} \chi^4 + J_{\text{sym}} \delta^2 + L_{\text{sym}} \delta^2 \chi + \frac{1}{2!} K_{\text{sym}} \delta^2 \chi^2 + \mathcal{O}(\chi^5, \chi^3 \delta^2), \quad (7)$$

where $\rho = \rho_n + \rho_p$ is the baryonic density with $\rho_{n(p)}$ denoting the neutron (proton) density, $\chi = (\rho - \rho_{\text{sat}})/3\rho_{\text{sat}}$, and $\delta = (\rho_n - \rho_p)/\rho$ is the isospin asymmetry.

The coefficients in the first line of the expansion (7) are known as isoscalar characteristics, namely, the *saturation energy* E_{sat} , the *incompressibility* K_{sat} , the *skewness* Q_{sat} , and the *kurtosis* Z_{sat} . The isovector characteristics (in the second line) associated with the density dependence of symmetry energy are the *symmetry energy parameter* J_{sym} , its *slope parameter* L_{sym} , and the *curvature* K_{sym} . The higher-order terms in the expansion (7), which are not shown here, have been studied, for example, in Refs. [13, 28, 29, 66].

To further specify the properties of a CDF, one needs additionally the value of the Dirac mass M_{D}^* at the saturation density, which is important for a quantitative description of the physics of finite nuclei. Consequently, in the present CDF framework, the seven adjustable parameters in Eq. (6) can be converted to seven macroscopic characteristics

$$\theta_{\text{EOS}} = (M_{\text{D}}^*, \rho_{\text{sat}}, E_{\text{sat}}, K_{\text{sat}}, Q_{\text{sat}}, J_{\text{sym}}, L_{\text{sym}}). \quad (8)$$

In particular, one could individually consider one of the quantities in Eq. (8) while fixing the others [67–69]. The mean values and standard deviations, or the respective parameter intervals, suggested by various works are summarized in Table II. Notably, we consider a broad range for Q_{sat} and L_{sym} that reflects the uncertainty of their values that exist in the literature [47, 48, 60–63, 66, 69].

In addition, we incorporate χ EFT results for pure neutron matter (PNM) in the density range 0.5–1.1 ρ_{sat} which constrain further the low-density regime of nucleonic EOS. In practice, we use the N³LO computations for the energy per particle and pressure from Ref. [41] at discrete density points (i.e., 0.08, 0.12 and 0.16 fm^{-3}) and assume the uncertainty as a Gaussian distribution at 1σ . Note that the uncertainty band reported in Ref. [41] lies fully within the bands predicted by various χ EFT based computations as compiled in Refs. [44, 70].

Next, we define likelihood functions for the aforementioned constraints for our analysis. For quantities with greater uncertainties, namely, Q_{sat} and L_{sym} , we adopt a pass-band selection which rejects models featuring values outside that range given in Table II. For quantities that are known to within approximately 10% or are given via the χ EFT computations, we assume two types of prior distributions.

TABLE II. Symmetric nuclear matter (SNM) characteristics at saturation density and pure neutron matter (PNM) properties from χ EFT that are used to constrain the CDF parameters.

	No.	Quantity	Unit	Interval
SNM	1	M_{D}^*	m_{N}	0.60 ± 0.05
	2	ρ_{sat}	fm^{-3}	0.153 ± 0.005
	3	E_{sat}	MeV	-16.1 ± 0.2
	4	K_{sat}	MeV	230 ± 40
	6	J_{sym}	MeV	32.5 ± 2.0
	5	Q_{sat}	MeV	$[-1400, 1400]$
	7	L_{sym}	MeV	$[0, 120]$
PNM	8	$P(\rho)$	MeV fm^{-3}	N ³ LO
	9	$\epsilon(\rho)$	MeV fm^{-3}	N ³ LO

(1). Gaussian distribution (abbreviated as ‘‘Gaus.’’). We assume a Gaussian prior distributions for each quantities, and the likelihood function reads

$$\mathcal{L}_{\text{NM}}(\theta_{\text{EOS}}) = \frac{1}{\sqrt{2\pi}\sigma} \exp\left[-\frac{1}{2}\left(\frac{\mu(\theta_{\text{EOS}}) - d}{\sigma}\right)^2\right], \quad (9)$$

where d and σ are the data and its standard uncertainties, respectively, and μ the corresponding model value.

(2). Uniform-Gaussian combination (abbreviated as UG). We assume a flat distribution that is centered on the assigned mean value for each quantity with a width of 2σ or 4σ interval, where the 1σ value is the one listed in Table II. Above or below the interval, the probabilities decay slowly as for a Gaussian function. Specifically, the likelihood function is defined as

$$\mathcal{L}_{\text{NM}}(\theta_{\text{EOS}}) = \begin{cases} \mathcal{L}_{\text{U}}(\mu), & d_{\text{min}} \leq \mu \leq d_{\text{max}} \\ \mathcal{L}_{\text{G}}(\mu), & \text{otherwise} \end{cases}, \quad (10)$$

where $\mathcal{L}_{\text{G}}(\mu)$ is the Gaussian function defined in Eq. (9), $\mathcal{L}_{\text{U}}(\mu)$ is a constant for which we introduce two cases. In UG1,

$$\mathcal{L}_{\text{U}}(\mu) = \frac{0.6827}{2\sigma}, \quad d - \sigma \leq \mu \leq d + \sigma, \quad (11)$$

and for UG2,

$$\mathcal{L}_{\text{U}}(\mu) = \frac{0.9545}{4\sigma}, \quad d - 2\sigma \leq \mu \leq d + 2\sigma. \quad (12)$$

In this way, we do not immediately discard all the models that are outside the 1σ or 2σ limit preassigned for the quantities in Table II, the samples are spanned in the same parameter space as the case with a Gaussian function. Furthermore, the distribution function (10) remains normalized, which thus allows the implementation of a quantitative comparison of the results obtained from different likelihoods.

B. Astrophysical constraints and the likelihoods

We next describe our implementations of the likelihoods for various CS measurements, and assume that the datasets of different observed sources are independent.

TABLE III. The astrophysical constraints used for the scenarios in the present analysis. For the four NICER sources the pulse profile models used to generate the samples are indicated.

Scenario	J0348	GW		J0740 ST-U	J0437 CST+PDT	J0030		J1231	
		170817	190425			ST+PDT	PDT-U	PDT-U (i)	PDT-U (ii)
Baseline	×	×							
B	×	×	×	×	×	×		×	
F	×	×	×	×	×		×		×

Massive millisecond pulsars (MP). The mass measurements of massive pulsars establish a rigorous lower bound on the maximum mass of a static CS, M_{\max} . We choose the most accurate mass value measured through Shapiro delay for PSR J0348+0432 [71], and assume the mass as a Gaussian distribution. The likelihood is constructed using the cumulative density function of the Gaussian function

$$\mathcal{L}_{\text{MP}}(\theta_{\text{EOS}}) = \frac{1}{2} \left[1 + \text{erf} \left(\frac{M_{\max}(\theta_{\text{EOS}}) - M}{\sqrt{2}\sigma} \right) \right], \quad (13)$$

where $\text{erf}(x)$ is the error function, M and σ are the mean and the standard deviation of the mass measurement for the source, respectively.

Gravitational waves data (GW). The GW170817 [72, 73] and GW190425 [74] events are the only two confirmed—and most likely—binary neutron star mergers observed during previous LIGO-Virgo-KAGRA observing runs. We calculate the likelihood through the high-precision interpolation in TOAST [75] that were obtained from fitting the strain data,

$$\mathcal{L}_{\text{GW}}(\theta_{\text{EOS}}) = F(\mathcal{M}, q, \Lambda_1, \Lambda_2), \quad (14)$$

where $\mathcal{M} = (M_1 M_2)^{3/5} / (M_1 + M_2)^{1/5}$ is the chirp mass, $q = M_1/M_2$ is the mass ratio, and $\Lambda_1(M_1)$ and $\Lambda_2(M_2)$ the tidal deformability of the individual star, respectively.

NICER data. The NICER collaboration has provided simultaneous measurements of mass and radius for four millisecond pulsars through pulse profile modeling: a massive $\sim 2.1 M_{\odot}$ star PSR J0740+6620 [76], two canonical-mass $\sim 1.4 M_{\odot}$ stars PSR J0030+0451 [77] and J0437-4715 [78], and a low-mass $\sim 1.1 M_{\odot}$ one PSR J1231-1411 [79]. We construct our likelihood function for each of the sources using the Gaussian kernel density estimation (KDE) with the released model posterior samples \mathcal{S} ,

$$\mathcal{L}_{\text{NICER}}(\theta_{\text{EOS}}) = \text{KDE}(M, R | \mathcal{S}), \quad (15)$$

where the mass M and radius R for the star are functions of its central pressure (equivalently, central density) and of the sampled EOS parameters.

In the present analysis, we implement the reported (M, R) samples as listed in Table III. For details of the pulse profile modelings, see Refs. [76–79]. Note that the reanalysis of PSR J0030+0451 resulted in three different ellipses in the M - R plane, each corresponding to a different pulse profile modeling [77]. For PSR J1231-1411, the inference results show a strong sensitivity to the choice of radius priors, with stable and likely converged outcomes achieved only under constrained

radius priors [79]. In this context, we propose scenarios B and F in Table III to represent two distinct combinations of the current NICER estimates for pulsars, corresponding to the softest and stiffest models, respectively (see also Refs. [33, 35]). Additionally, we introduce the Baseline scenario, which incorporates a minimal set of astrophysical constraints—specifically, the mass of PSR J0348+0432 and the tidal deformabilities from GW170817. Below, we perform illustrative tests using these three scenarios.

IV. RESULTS AND IMPLICATIONS

We now assess the current theoretical uncertainties arising from the choice of likelihood functions used to constrain low-density matter and examine their implications for the proper-

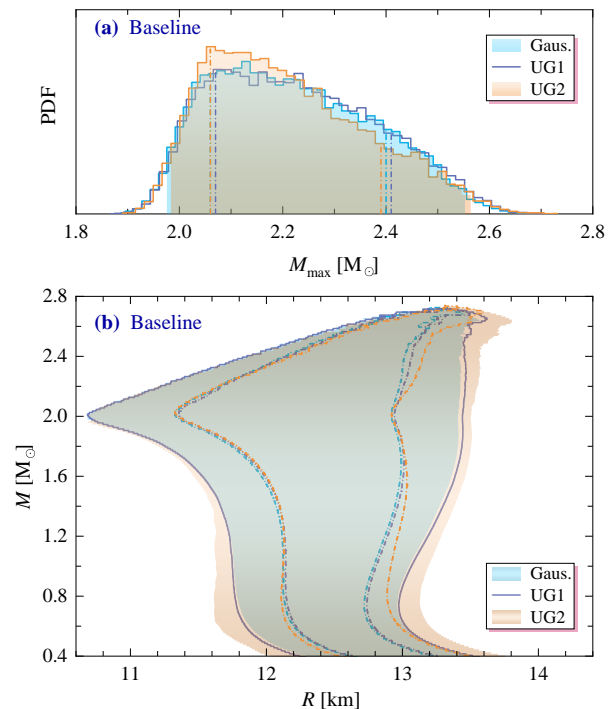


FIG. 1. Posterior distributions for mass-radius relations and maximum mass under the Baseline astrophysical scenario, assuming low-density matter constraints are modeled using either a Gaussian likelihood (Gaus.) or a hybrid of uniform and Gaussian distributions (UG1 and UG2). Shaded regions indicate the 95.4% confidence intervals (CIs), while solid lines represent the 68.3% CIs.

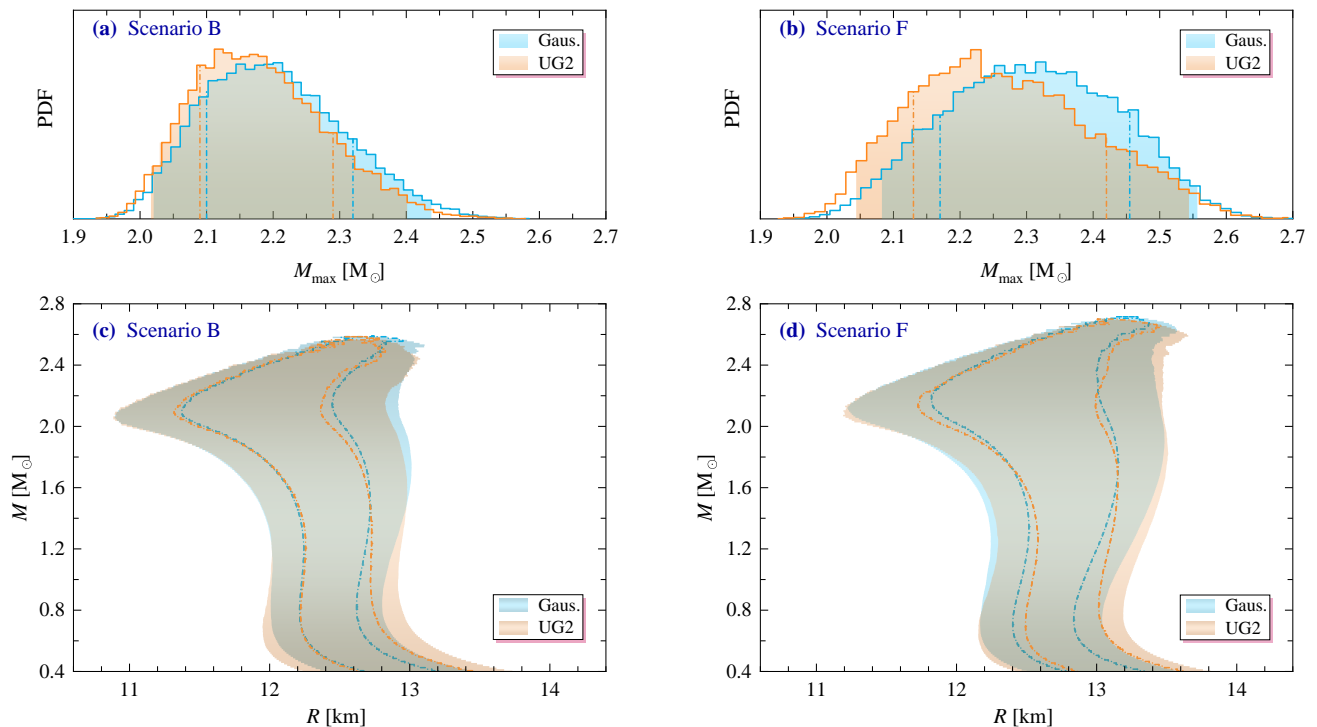


FIG. 2. Posterior distributions for the mass-radius relation and maximum mass under astrophysical scenarios B (left panels) and F (right panels), assuming low-density matter constraints modeled using either a Gaussian likelihood (Gaus.) or a combined uniform-Gaussian distribution (UG2). Shaded regions correspond to the 95.4% confidence intervals (CIs), while the lines indicate the 68.3% CIs.

ties of compact stars and dense matter. Our statistical analysis is based on approximately 3×10^4 posterior EOS models that satisfy both nuclear theory and observational constraints from pulsar and gravitational-wave measurements.

A. Properties of compact stars

We begin by evaluating the impact of different likelihood choices for low-density matter constraints on the properties of compact stars, assuming either a Gaussian prior (Gaus.) or a combination of uniform and Gaussian priors (UG1 or UG2). The bulk properties of CSs—such as their maximum mass, radii, tidal deformabilities, and moments of inertia—are entirely determined by the distributions of energy density and pressure throughout the star, as prescribed by the EOS of dense matter. However, these properties are integrated quantities, meaning they are sensitive to how pressure and energy density are distributed across the full range of densities within the star.

In Fig. 1, we present the $M-R$ posteriors and the probability distribution functions (PDFs) for maximum mass M_{\max} under scenario “Baseline”, for which the 68.3% and 95.4% confidence intervals (CIs) are indicated. Physically, the mass $\sim 2 M_{\odot}$ of PSR J0348+0432 sets a lower bound on the maximum mass M_{\max} , thus provides the most rigorous constraint on the high-density behavior of the EOS of dense stellar matter; the tidal deformabilities deduced from GW170817 event places additional constraints on the intermediate range

of EOS. It is clearly seen from Fig. 1 that the two posteriors are almost identical for computations with Gaussian and UG1 likelihood functions, both at 68.3% and 95.4% CIs. Such consistency is further established from the specific values of key gross quantities of CSs and the characteristic parameters of nuclear matter at saturation density, which are collected in the Appendix. The differences for each quantities between the two approaches are well within 1%. A similar conclusion was reached in Ref. [31], where the two types of likelihood functions were applied exclusively to the χ EFT constraints.

In light of the above results, from now on, our comparative study shall be concentrated on the computations with a wider uniform distribution, i.e., the results obtained from UG2 likelihood function. In this case, as shown in Fig. 1, the $M-R$ posterior region broadens noticeably by approximately 0.2 km on both sides. For masses $M \lesssim 1.6 M_{\odot}$, this widening is primarily due to the broader range of EOSs at low densities ($\rho \lesssim 2\rho_{\text{ast}}$) permitted by the looser χ EFT constraint under the UG2 likelihood. This allows models with more extreme values of the isovector parameters J_{sym} and L_{sym} to contribute to the posterior—parameters that play a key role in determining the radii of low-mass stars.

Meanwhile, a lower value of L_{sym} can be offset by a higher value of the isoscalar parameter Q_{sat} [67], resulting in a viable model within the current framework. The parameter Q_{sat} predominantly influences the radii of high-mass stars ($M \gtrsim 1.6 M_{\odot}$) as well as the maximum mass of compact stars [68]. The posterior distributions of the nuclear matter characteristics will be discussed in the following subsection.

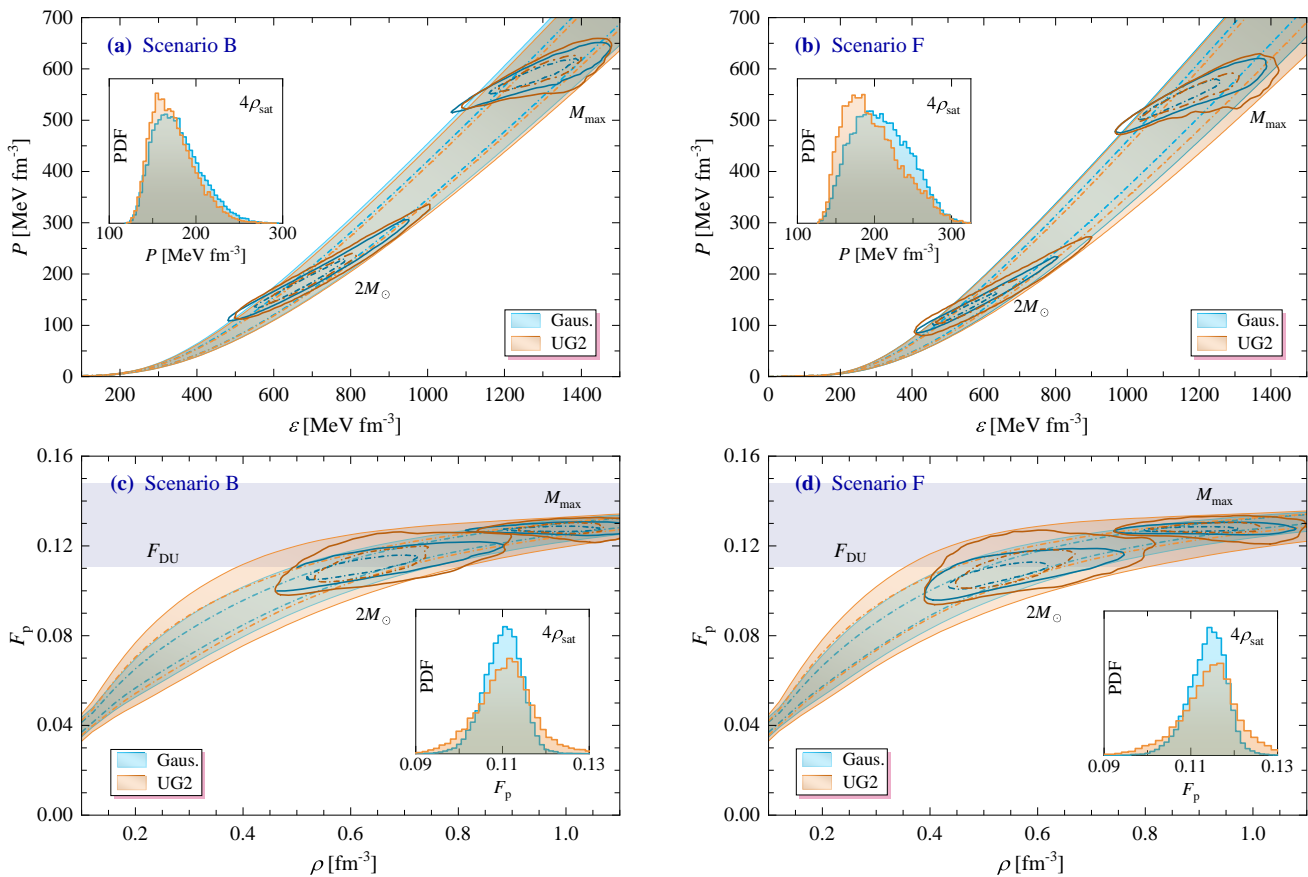


FIG. 3. Posteriors for β -stable EOS and proton fraction distributions under astrophysical scenarios B (left panels) and F (right panels), assuming for the low-density matter constraints a likelihood of Gaussian distribution (Gaus.) or a combination of uniform and Gaussian distributions (UG2). The shaded regions represent the distributions at 95.4% confidence intervals (CIs) while the lines for 68.3% CIs. In each panel, the contours indicate the corresponding distributions of the respective $2.0 M_{\odot}$ and the maximum mass M_{\max} configurations, and the insets show the PDFs of the pressure or fraction at $4\rho_{\text{sat}}$. In lower panels the orange band labeled F_{DU} shows the admissible threshold values for the onset of nucleonic direct Urca (DU) cooling process.

The combined NICER and XMM-Newton measurements of both the radii and masses of four pulsars [76–83], with masses ranging from approximately 1.0 to $2.1 M_{\odot}$, along with the tidal deformabilities inferred from the GW170817 and GW190425 binary neutron star merger events [72, 74], provide a valuable opportunity to constrain the dense matter equation of state at densities between 2 and 4 times ρ_{sat} . We present illustrative results for scenarios B and F in Fig. 2, after incorporating NICER data for four pulsars into our analysis. In scenario B, we use more compact estimates for PSR J0030+0451 (ST+PDT model) and PSR J1231-1411 (PDT-U (i) model), which favor softer equations of state at densities below ~ 2 and $3\rho_{\text{sat}}$, respectively, resulting in the tightest credible regions. In contrast, scenario F, which incorporates less compact estimates for PSR J0030+0451 (PDT-U model) and PSR J1231-1411 (PDT-U (ii) model), predicts the widest credible regions. In the lower panels of Fig. 2, we observe that the impacts of the likelihood functions for low-density matter constraints on the M - R distributions are largely suppressed. With a Gaussian prior (Gaus.) or a combination of uniform and Gaussian distributions (UG2), the differences in

radii for stars with masses $M \gtrsim 1 M_{\odot}$ are well within 0.1 km. In contrast, for computations using UG2 likelihood functions, the predicted maximum masses are shifted to lower values by at most $0.05 M_{\odot}$ compared to those obtained using Gaussian likelihoods, as shown in the upper panels of Fig. 2. Additionally, in scenario F, computations with UG2 likelihood functions still permit maximum masses exceeding $2.5 M_{\odot}$ at the 95.4% confidence interval, thus supporting a static compact star interpretation for the secondary component of the GW190814 event [84].

The inferred key quantities of CSs, such as radii, tidal deformabilities, central baryonic densities, energy densities, pressures, sound speeds ($c_s^2 = dP/d\varepsilon$), and the dimensionless trace anomalies ($\Delta = 1/3 - P/\varepsilon$) [85] for 1.0, 1.4, $2.0 M_{\odot}$ and the maximum-mass configuration are collected in the Appendix.

Figure 3 summarizes the posterior distributions for β -equilibrium EOS that generated the posteriors in Fig. 2, as well as the corresponding proton fraction. In each panel, we also show the contours representing the positions of the respective $2.0 M_{\odot}$ and the maximum-mass M_{\max} configurations, and the PDFs of the pressure or fraction at $4\rho_{\text{sat}}$. In the lower

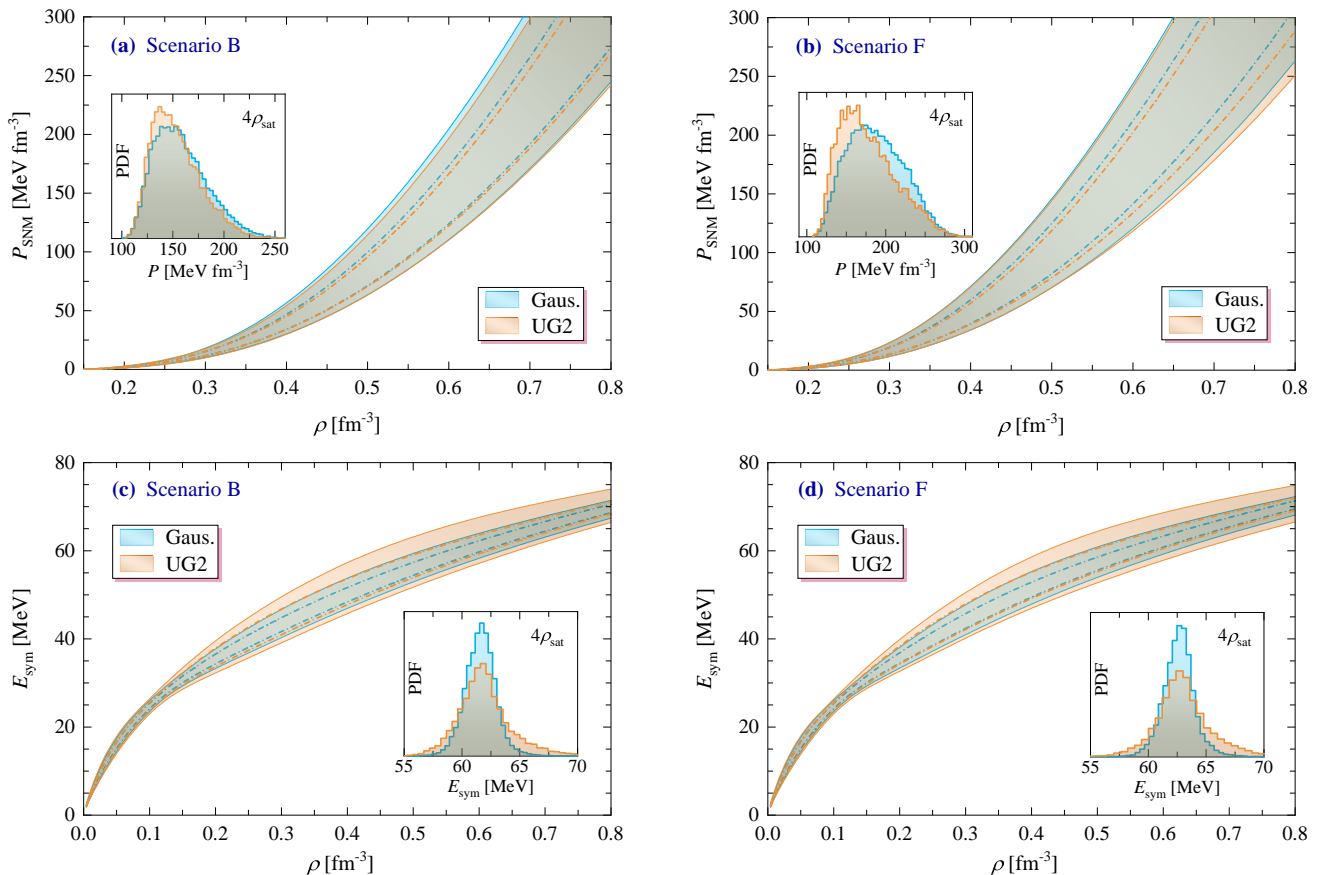


FIG. 4. Posterior distributions for nucleonic equations of state (EOS) and symmetry energy under astrophysical scenarios B (left panels) and F (right panels), assuming low-density matter constraints are modeled using either a Gaussian likelihood (Gaus.) or a combined uniform-Gaussian distribution (UG2). Shaded regions indicate the 95.4% confidence intervals (CIs), while lines represent the 68.3% CIs. Insets in each panel display the probability density functions (PDFs) of the pressure or symmetry energy at $4\rho_{\text{sat}}$.

panels of Fig. 3 the horizontal bands indicate the nucleonic direct Urca (DU) threshold for the compact star cooling process. The lower limit of 11.1% is derived from the μ^- free model, while the upper limit comes from a model which assumes massless μ , which, however, applies only in high-density matter [86].

As seen in the upper panels of Fig. 3, both computations for scenarios B and F yield consistent results with Gaussian or UG2 likelihood functions. The analyses with UG2 likelihoods favor a slightly softer equation of state, as indicated by the insets, where the peaks of the pressure PDFs are shifted toward lower values for a fixed baryonic density.

As shown in the lower panels of Fig. 3, the analyses with UG2 likelihoods result in a broader proton fraction distribution, due to modifications in the value of the symmetry energy slope L_{sym} (which will be discussed in the next section). However, these modifications do not alter our previous conclusion [33, 35] that the DU process is largely disallowed in compact stars with $M < 2.0 M_{\odot}$ when using the current CDF-based EOS. A similar conclusion was reached in Refs. [21, 34], where the density dependence of the ρ -meson coupling was also modeled using an exponential form, see Eq. (5).

B. Properties of nucleonic matter

Next, we assess the impact of the likelihoods for low-density matter constraints on the properties of symmetric nuclear matter and the density dependence of symmetry energy.

In Fig. 4, we display the posterior distributions for pressure (upper panels) and symmetry energy (lower panels) as a function of baryonic density under astrophysical scenarios B and F. We assume a Gaussian distribution (Gaus.) for the low-density matter constraints or a combination of uniform and Gaussian distributions (UG2). In each panel we also illustrate the probability density functions (PDFs) at a density of $4\rho_{\text{sat}}$. The upper panels of Fig. 4 show consistency with the β -stable EOS presented in Fig. 3, indicating that analyses using the UG2 likelihood slightly favor a softer symmetrical matter EOS. For the symmetry energy, the UG2 likelihood function results in a broad distribution, particularly in high-density regions. However, the variations in symmetry energy values remain below 3 MeV across the relevant density ranges, which may not significantly impact the properties of CSs.

In Fig. 5 we display the posterior distributions for nine nuclear characteristics, see Eq. (7), at saturation density under scenarios B (left panels) and F (right panels). Note that the

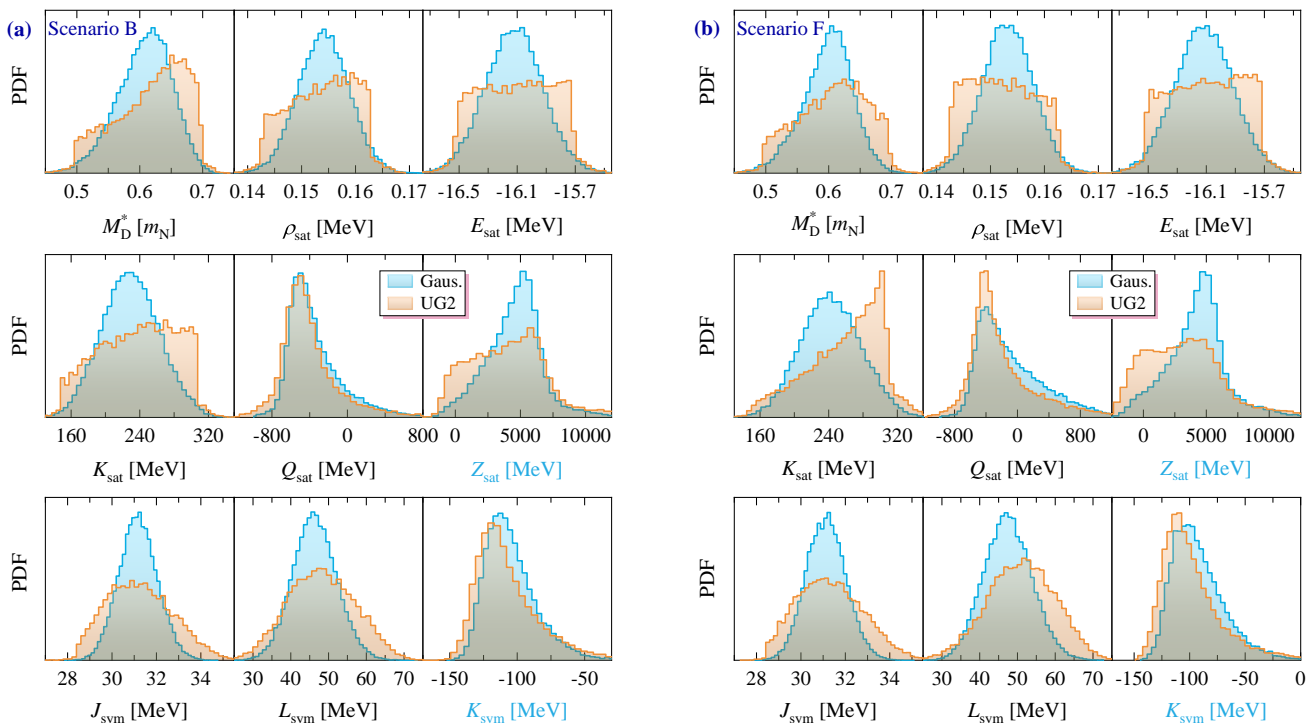


FIG. 5. Posterior distributions for nuclear matter properties at saturation density under astrophysical scenarios B (left panels) and F (right panels), assuming low-density matter constraints modeled using either a Gaussian likelihood (Gaus.) or a combined uniform-Gaussian distribution (UG2). The higher-order parameters Z_{sat} and K_{sym} , shown in blue, are predicted from the lower-order parameters within the present CDF framework.

higher-order parameters Z_{sat} and K_{sym} are predictions of those lower-order parameters that uniquely determine the CDF. We conclude that the likelihood functions used for low-density matter constraints affect mainly the predictions for the distributions of nuclear characteristics.

In Fig. 6, we show the posterior correlation matrix for variations in nuclear characteristic parameters at saturation density, along with selected gross properties of CSs under the astrophysical scenario F, using two different likelihoods for low-density matter constraints. Scenario B yields similar findings. This figure also includes the dimensionless trace anomaly and the squared sound speed. The inferred nuclear characteristics at saturation density are compiled in the appendix, where we provide the parameters for each isospin sector up to fourth order in the expansion with respect to the density. In this work we use Pearson's correlation coefficient defined as

$$r_{XY} = \frac{\text{cov}(X, Y)}{\sigma_X \sigma_Y},$$

where σ_X is the standard deviation of X , $\text{cov}(X, Y)$ is the covariance between variables X and Y ,

$$\text{cov}(X, Y) = \frac{1}{n} \sum_i^n (X_i - \bar{X})(Y_i - \bar{Y}),$$

with n the number of samples and \bar{X} denotes the mean of variable X .

From Figs. 5 and 6, the following systematics are observed:

(1). The posterior distributions for the three fundamental parameters, M_D^* , ρ_{sat} , and E_{sat} , are quite similar to their prior distributions. This is especially evident for ρ_{sat} and E_{sat} , suggesting that they are not important for the high-density properties of EOS. This conclusion is further supported by the correlation matrix shown in Fig. 6, where the absolute values of the Pearson correlation coefficients (r) between E_{sat} (ρ_{sat}) and the radii of selected stars, as well as the maximum mass M_{max} , are relatively low, with r less than 0.3.

(2). Another important observation is that in the UG2 approach, the Dirac mass M_D^* tends to be higher in both scenarios B and F, with a more significant increase for the PDFs in scenario B. This can likely be explained by the Hugenholtz-van-Hove theorem, applied at saturation density. It states that at zero temperature the Fermi energy equals the energy per particle at saturation [87, 88]. Specifically, larger M_D^* which correspond to small σ -meson field, requires a weaker ω -meson field. Indeed, the Fermi energy is expressed as (disregard the rearrangement in the interaction)

$$E_F = g_\omega \bar{\omega} + \sqrt{k_F^2 + M_D^{*2}}.$$

where E_F denotes the saturation energy, which is known to within approximately 5% and $\bar{\omega}$ is the mean-field expectation value. An increase in the Dirac effective mass (corresponding to a reduction in the scalar potential) requires a smaller vector potential given by $g_\omega \bar{\omega}$. Consequently, this leads to a softer EOS at high densities, where the contribution from

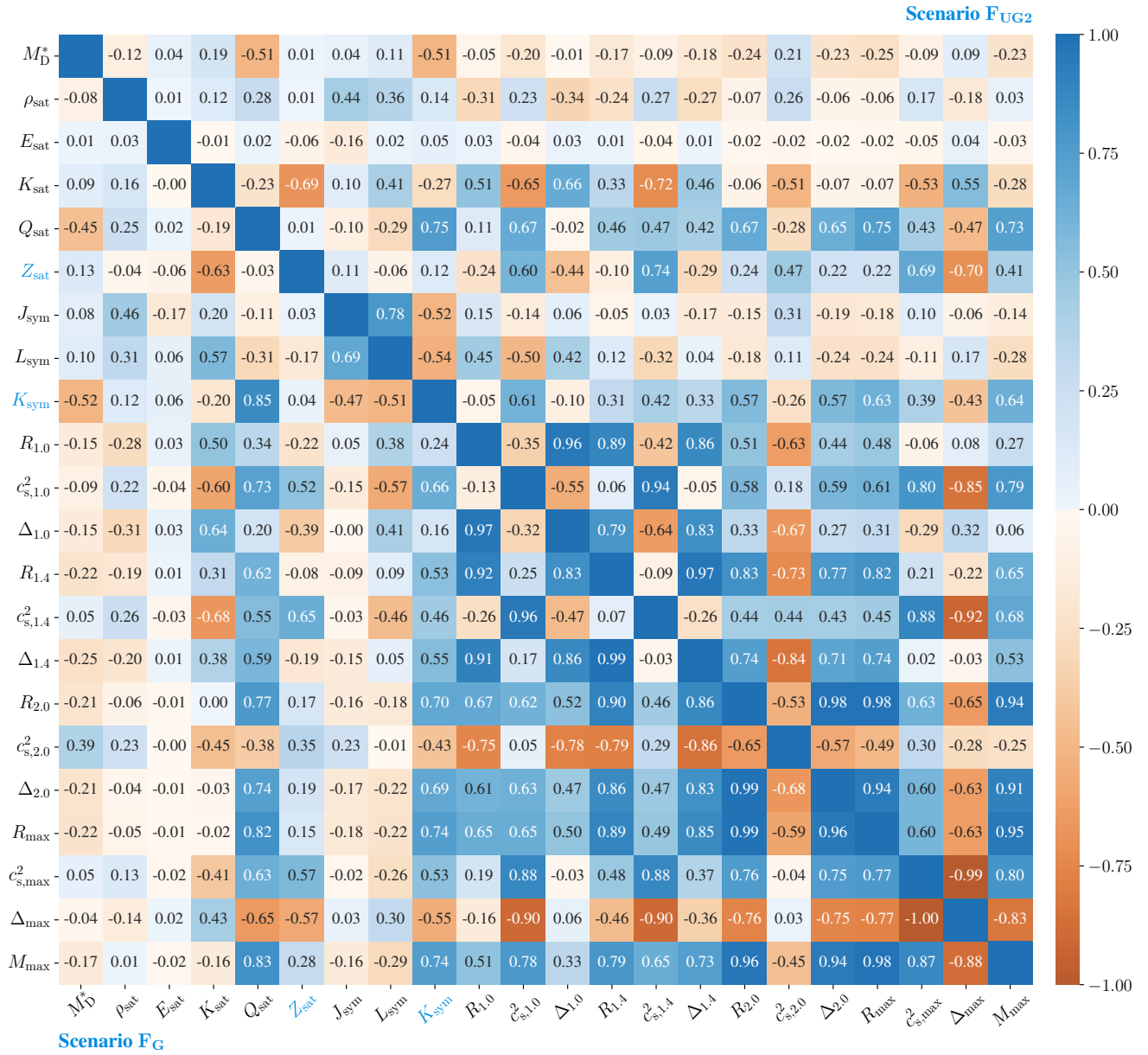


FIG. 6. Posterior correlation matrix showing the variation of nuclear characteristic parameters at saturation density and selected bulk properties of compact stars under astrophysical scenario F. The lower-left part corresponds to constraints modeled with a Gaussian likelihood (G), while the upper-right reflects a combined uniform-Gaussian distribution (UG2). Higher-order parameters Z_{sat} and K_{sym} , highlighted in blue, are predicted from lower-order parameters within the current CDF framework.

the ω -meson dominates the behavior of the EOS. This results in a softer EOS as required by observational constraints in scenario B. Additionally, it is important to note a moderate anti-correlation ($r \approx -0.5$), shown in Fig. 6, between the parameters M_D^* and Q_{sat} , where the values of Q_{sat} derived from UG2 likelihoods are somewhat lower than those obtained using Gaussian likelihoods.

(3). The isoscalar incompressibility K_{sat} is highly sensitive to the likelihood functions and the observational constraints. In scenario B, the posterior distribution for K_{sat} is almost uniform across most of the distribution range when using the UG2 likelihood. In contrast, scenario F shows an exponen-

tial increase in the posterior, peaking near the upper limit of the uniform prior at $K_{\text{sat}} = 310$ MeV. In both scenarios, the UG2 approach produces wider 68.3% and 95.4% CI posterior ranges compared to the Gaussian approach (see the specific values in the Appendix).

(4). In both scenarios B and F, the isoscalar skewness values, Q_{sat} , computed using the UG2 approach are somewhat lower compared to those obtained from the Gaussian approach. This adjustment is made to balance the effect of the higher K_{sat} values that the UG2 approach tends to favor. For example, in scenario B, the median value of K_{sat} increases by 12 MeV when transitioning from the Gaussian to the UG2 approaches,

while the Q_{sat} values decrease by approximately 45 MeV. Note also that the coefficients in front of K_{sat} and Q_{sat} in Eq. (7) differ by a factor of 1/3. We emphasize once more that Q_{sat} is the primary parameter dominating the maximum mass of CSs within the current CDF framework.

(5). The posteriors for the isovector parameters J_{sym} and L_{sym} still display Gaussian-like behaviors, even though the majority of the prior intervals are assumed to have uniform distributions (UG2). This behavior is due to the strong correlation between the two parameters when the χEFT constraint is applied. This is established in the correlation matrix shown in Fig. 6, where the Pearson correlation coefficient for the pair ($J_{\text{sym}}, L_{\text{sym}}$) is $r \approx 0.7$ in both approaches for the likelihoods.

(6). Similar to the counterbalancing behavior between the isoscalar parameters K_{sat} and Q_{sat} , the slightly higher values of L_{sym} favored by the UG2 approach lead to an increase in the next-order isovector parameter, K_{sym} , in order to keep the isovector sector of the EOS less sensitive to the choice of likelihood. However, it is important to note that within the current CDF framework, variations in K_{sym} primarily arise from adjustments to the lower-order isovector parameters J_{sym} and L_{sym} .

Furthermore, we observe that the 95.4% CI for K_{sat} , obtained using the UG2 approach under scenario F, is shifted upward by approximately 20 MeV compared to the interval derived with a uniform prior. Although both intervals have comparable widths, this systematic shift toward higher values underscores important considerations for parameter estimation. In particular, the observed discrepancy highlights the need to carefully account for marginalization effects when employing uniform likelihood functions in Bayesian analyses. These results suggest that, unless the prior range is sufficiently broad, inadequate treatment of marginalization can introduce unintended biases in the posterior inference.

Finally, we return to the analysis of Fig. 6. The overall correlation structure among nuclear matter characteristics shows remarkable consistency between the two approaches. However, distinct differences emerge in specific parameter correlations: the absolute correlations between nuclear incompressibility K_{sat} and CS properties are noticeably enhanced when using the UG2 likelihood function, compared to those derived from the Gaussian likelihood. In contrast, the correlation strengths involving the skewness parameter Q_{sat} exhibit significant attenuation under the UG2 approach. This behavior suggests a compensatory mechanism in the EOS parametrization, where these two parameters tend to offset each other's influence. In conclusion, our findings illustrate that the integrated nature of CS bulk properties inherently masks detailed information about individual nuclear parameters. Therefore, dedicated nuclear experiments specifically sensitive to K_{sat} and L_{sym} are essential for constraining their values more precisely.

V. CONCLUSIONS

In this work, we performed a systematic comparison of Bayesian inference outcomes for CDF-type EOS of dense matter, focusing on the impact of likelihood functions between Gaussian and uniform distributions when incorporating low-density matter constraints. While both likelihood formulations are routinely utilized in Bayesian analyses, we introduce critical modifications to ensure methodological equivalence: the uniform likelihood is augmented with a normalization factor and a Gaussian-inspired tail. In both approaches, the EOS models have been built with identical priors for the CDF parameters, and employ the same methods to construct the likelihood for observational constraints.

In our analysis, we have assessed how the two inferences differ by testing the gross properties of CSs and dense matter EOS, and the correlations among them, under three astrophysical scenarios providing looser and tighter constraints, respectively. We have found that the two approaches lead to very similar posterior results for the gross properties of CSs (e.g., maximum mass, radii, and tidal deformabilities) and dense matter (e.g., EOS, sound speed, and trace anomaly) with the 95.4% CI essentially overlapping. The difference in particle composition is statistically negligible and can be safely neglected without noticeable effect.

Notable discrepancies emerge in the nuclear matter characteristics at saturation density. Parameters such as the saturation density ρ_{sat} and energy per particle E_{sat} , which are largely independent of observational constraints, retain prior-dominated distributions. In contrast, the incompressibility modulus K_{sat} shows high sensitivity to both its likelihood function and the observational data, while the isoscalar skewness Q_{sat} adjusts accordingly to preserve the consistency of the predictions of the EOS. In the isovector sector, the parameters J_{sym} and L_{sym} maintain a strong mutual correlation, even though their individual distributions vary depending on the choice of likelihood function. These findings highlight the fact that the integrated nature of compact star gross properties tends to obscure direct information about individual nuclear parameters close to saturation.

ACKNOWLEDGMENTS

J. J. L. acknowledges the support of the National Natural Science Foundation of China under Grants No. 12105232 and No. 12475150. A. S. acknowledges funding by the Deutsche Forschungsgemeinschaft Grant No. SE 1836/6-1 and the Polish NCN Grant No. 2023/51/B/ST9/02798.

Appendix: Key quantities of nuclear matter and compact stars

In this appendix, we present the characteristic parameters of nuclear matter at saturation density and key gross quantities of CSs predicted by CDFs for the three astrophysical scenarios, assuming for the low-density matter constraints a likelihood of Gaussian distribution (Gaus.) or a combination of uniform and Gaussian distributions (UG1 or UG2).

TABLE IV. Characteristic parameters of symmetric nuclear matter at saturation density from the posterior distributions for astrophysical scenarios Baseline, B and F with different likelihoods for low-density matter constraints. The superscripts and subscripts indicate the 68.3% and 95.4% (in brackets) CI ranges.

Par.	Unit	Baseline			Scenario B		Scenario F	
		Gaus.	UG1	UG2	Gaus.	UG2	Gaus.	UG2
M_D^*	m_N	$0.609^{+0.041(0.081)}_{-0.043(0.091)}$	$0.610^{+0.039(0.079)}_{-0.049(0.094)}$	$0.618^{+0.056(0.080)}_{-0.071(0.113)}$	$0.614^{+0.039(0.072)}_{-0.047(0.098)}$	$0.630^{+0.047(0.068)}_{-0.076(0.125)}$	$0.605^{+0.035(0.070)}_{-0.043(0.091)}$	$0.614^{+0.053(0.083)}_{-0.067(0.110)}$
ρ_{sat}	fm^{-3}	$0.154^{+0.020(0.040)}_{-0.005(0.009)}$	$0.154^{+0.020(0.040)}_{-0.005(0.009)}$	$0.154^{+0.020(0.040)}_{-0.007(0.011)}$	$0.154^{+0.020(0.040)}_{-0.005(0.009)}$	$0.155^{+0.020(0.040)}_{-0.008(0.011)}$	$0.154^{+0.020(0.040)}_{-0.005(0.009)}$	$0.152^{+0.020(0.040)}_{-0.007(0.009)}$
E_{sat}	MeV	$-16.10^{+0.20(0.40)}_{-0.20(0.40)}$	$-16.11^{+0.20(0.40)}_{-0.20(0.40)}$	$-16.09^{+0.28(0.39)}_{-0.30(0.41)}$	$-16.10^{+0.20(0.40)}_{-0.20(0.40)}$	$-16.08^{+0.28(0.40)}_{-0.29(0.40)}$	$-16.10^{+0.20(0.40)}_{-0.20(0.40)}$	$-16.08^{+0.27(0.38)}_{-0.29(0.42)}$
K_{sat}	MeV	$231.5^{+38.1(74.7)}_{-35.5(70.4)}$	$233.9^{+37.2(72.2)}_{-39.1(73.4)}$	$244.7^{+49.3(67.8)}_{-60.2(91.5)}$	$231.4^{+34.4(68.7)}_{-33.3(64.0)}$	$243.0^{+46.9(66.0)}_{-54.2(88.1)}$	$244.8^{+36.4(71.2)}_{-34.7(67.8)}$	$270.7^{+33.6(61.2)}_{-56.5(105.6)}$
Q_{sat}	MeV	$-361.5^{+563.1(1245.5)}_{-229.7(377.0)}$	$-354.7^{+569.4(1322.8)}_{-228.6(378.0)}$	$-393.7^{+548.4(1418.2)}_{-222.4(413.9)}$	$-391.0^{+333.6(872.8)}_{-170.2(323.3)}$	$-436.0^{+548.9(161.9)}_{-183.7(434.1)}$	$-164.7^{+304.2(909.1)}_{-280.1(455.4)}$	$-298.5^{+515.8(1266.8)}_{-209.1(483.5)}$
Z_{sat}	MeV	$4866^{+1704(4920)}_{-2377(4978)}$	$4829^{+1818(5241)}_{-2482(4970)}$	$4294^{+2801(7626)}_{-3351(5020)}$	$4931^{+1595(4862)}_{-2330(4721)}$	$4386^{+2693(8369)}_{-3303(4920)}$	$4641^{+1663(5497)}_{-2508(5071)}$	$3367^{+2962(8739)}_{-3145(4818)}$
J_{sym}	MeV	$31.20^{+0.88(1.80)}_{-0.87(1.69)}$	$31.18^{+0.97(1.95)}_{-0.84(1.79)}$	$31.06^{+1.68(3.21)}_{-1.38(2.32)}$	$31.24^{+0.88(1.78)}_{-0.86(1.68)}$	$31.27^{+1.66(3.14)}_{-1.45(2.44)}$	$31.20^{+0.89(1.82)}_{-0.88(1.72)}$	$31.31^{+1.65(3.12)}_{-1.46(2.47)}$
L_{sym}	MeV	$46.28^{+6.33(13.13)}_{-5.91(11.44)}$	$46.89^{+6.18(12.33)}_{-6.75(12.95)}$	$47.82^{+10.05(18.74)}_{-9.58(17.84)}$	$46.73^{+5.94(13.00)}_{-5.67(11.35)}$	$48.63^{+9.46(17.39)}_{-8.84(16.79)}$	$47.86^{+6.46(13.08)}_{-6.27(12.15)}$	$51.73^{+9.06(16.72)}_{-9.04(18.35)}$
K_{sym}	MeV	$-103.1^{+27.8(63.3)}_{-18.5(31.5)}$	$-103.1^{+29.6(70.0)}_{-19.0(32.2)}$	$-104.0^{+34.6(91.9)}_{-20.8(34.8)}$	$-106.0^{+21.0(50.5)}_{-14.7(25.8)}$	$-110.0^{+27.9(73.1)}_{-15.8(27.7)}$	$-94.2^{+26.6(61.8)}_{-18.2(31.1)}$	$-101.8^{+30.2(83.4)}_{-17.7(30.9)}$
Q_{sym}	MeV	$792.8^{+155.9(289.6)}_{-173.0(351.8)}$	$776.2^{+172.6(313.7)}_{-166.5(336.2)}$	$715.4^{+233.6(423.6)}_{-215.5(406.7)}$	$776.1^{+155.8(295.8)}_{-159.1(323.0)}$	$702.0^{+212.5(409.9)}_{-194.7(366.3)}$	$765.3^{+166.5(299.3)}_{-177.0(358.4)}$	$624.8^{+225.7(440.4)}_{-180.4(361.6)}$
Z_{sym}	MeV	$-5369^{+1660(2840)}_{-2398(5401)}$	$-5302^{+1669(2763)}_{-2572(5952)}$	$-4887^{+2004(3066)}_{-3149(7570)}$	$-5079^{+1435(2523)}_{-1988(4606)}$	$-4402^{+1692(2587)}_{-2589(6298)}$	$-5686^{+1820(3095)}_{-2596(5565)}$	$-4401^{+1705(2630)}_{-3007(7611)}$

TABLE V. Key quantities of compact stars from the posterior distributions for astrophysical scenarios Baseline, B and F with different likelihoods for low-density matter constraints: radii, tidal deformabilities, central baryonic densities, energy densities, pressures, sound speeds, and trace anomalies for 1.0, 1.4, 2.0 M_{\odot} and the maximum-mass stars. The superscripts and subscripts indicate the 95.4% CI ranges.

Par.	Unit	Baseline			Scenario B		Scenario F	
		Gaus.	UG1	UG2	Gaus.	UG2	Gaus.	UG2
$R_{1.0}$	km	$12.47^{+0.58}_{-0.71}$	$12.51^{+0.58}_{-0.76}$	$12.56^{+0.63}_{-0.89}$	$12.44^{+0.38}_{-0.43}$	$12.50^{+0.42}_{-0.49}$	$12.69^{+0.43}_{-0.47}$	$12.81^{+0.43}_{-0.56}$
$\Lambda_{1.0}$		3162^{+1126}_{-995}	3222^{+1151}_{-1059}	3307^{+1213}_{-1189}	3114^{+667}_{-619}	3184^{+693}_{-700}	3554^{+858}_{-764}	3706^{+883}_{-840}
$\rho_{1.0}$	fm^{-3}	$0.339^{+0.076}_{-0.059}$	$0.336^{+0.078}_{-0.060}$	$0.334^{+0.082}_{-0.061}$	$0.342^{+0.044}_{-0.041}$	$0.341^{+0.046}_{-0.038}$	$0.316^{+0.047}_{-0.040}$	$0.315^{+0.045}_{-0.041}$
$P_{1.0}$	MeV/fm^3	$29.89^{+10.01}_{-6.66}$	$29.50^{+10.39}_{-6.65}$	$29.07^{+11.42}_{-6.61}$	$30.27^{+5.69}_{-4.52}$	$29.97^{+6.13}_{-4.32}$	$27.19^{+5.69}_{-4.43}$	$26.72^{+5.66}_{-4.32}$
$\varepsilon_{1.0}$	MeV/fm^3	$337.30^{+78.67}_{-61.49}$	$334.43^{+80.99}_{-61.96}$	$333.22^{+84.76}_{-62.90}$	$340.87^{+45.95}_{-42.40}$	$340.34^{+48.04}_{-40.02}$	$313.91^{+48.94}_{-41.88}$	$313.33^{+46.76}_{-42.73}$
$c_{s,1.0}^2$		$0.267^{+0.032}_{-0.043}$	$0.266^{+0.032}_{-0.045}$	$0.260^{+0.041}_{-0.045}$	$0.263^{+0.033}_{-0.037}$	$0.255^{+0.042}_{-0.046}$	$0.269^{+0.030}_{-0.044}$	$0.251^{+0.047}_{-0.039}$
$\Delta_{1.0}$		$0.245^{+0.005}_{-0.008}$	$0.245^{+0.005}_{-0.008}$	$0.246^{+0.006}_{-0.010}$	$0.244^{+0.004}_{-0.005}$	$0.245^{+0.004}_{-0.006}$	$0.247^{+0.004}_{-0.004}$	$0.248^{+0.004}_{-0.006}$
$R_{1.4}$	km	$12.51^{+0.77}_{-0.84}$	$12.55^{+0.78}_{-0.88}$	$12.58^{+0.80}_{-0.95}$	$12.47^{+0.48}_{-0.50}$	$12.49^{+0.48}_{-0.52}$	$12.79^{+0.55}_{-0.56}$	$12.84^{+0.56}_{-0.57}$
$\Lambda_{1.4}$		483^{+271}_{-189}	493^{+283}_{-198}	497^{+295}_{-206}	472^{+163}_{-121}	474^{+153}_{-124}	571^{+207}_{-162}	574^{+218}_{-156}
$\rho_{1.4}$	fm^{-3}	$0.420^{+0.113}_{-0.092}$	$0.416^{+0.116}_{-0.093}$	$0.419^{+0.114}_{-0.098}$	$0.425^{+0.070}_{-0.067}$	$0.429^{+0.067}_{-0.066}$	$0.384^{+0.078}_{-0.062}$	$0.391^{+0.069}_{-0.069}$
$P_{1.4}$	MeV/fm^3	$58.979^{+26.249}_{-17.626}$	$58.189^{+26.827}_{-17.601}$	$58.260^{+27.410}_{-18.156}$	$60.042^{+15.313}_{-12.859}$	$60.402^{+15.269}_{-12.345}$	$51.927^{+15.549}_{-11.458}$	$52.511^{+14.136}_{-12.267}$
$\varepsilon_{1.4}$	MeV/fm^3	$428.05^{+124.05}_{-99.64}$	$424.25^{+126.67}_{-100.70}$	$427.55^{+124.68}_{-105.79}$	$433.76^{+79.56}_{-73.38}$	$438.23^{+74.32}_{-71.62}$	$389.96^{+85.26}_{-68.82}$	$397.99^{+85.26}_{-73.01}$
$c_{s,1.4}^2$		$0.378^{+0.029}_{-0.052}$	$0.377^{+0.029}_{-0.052}$	$0.371^{+0.040}_{-0.058}$	$0.374^{+0.030}_{-0.046}$	$0.368^{+0.039}_{-0.050}$	$0.376^{+0.026}_{-0.054}$	$0.359^{+0.042}_{-0.057}$
$\Delta_{1.4}$		$0.196^{+0.012}_{-0.017}$	$0.196^{+0.012}_{-0.018}$	$0.197^{+0.012}_{-0.020}$	$0.195^{+0.008}_{-0.011}$	$0.195^{+0.008}_{-0.011}$	$0.200^{+0.008}_{-0.010}$	$0.202^{+0.008}_{-0.011}$
$R_{2.0}$	km	$12.15^{+1.26}_{-1.47}$	$12.19^{+1.28}_{-1.50}$	$12.12^{+1.38}_{-1.42}$	$12.04^{+0.91}_{-1.03}$	$12.00^{+0.90}_{-1.00}$	$12.60^{+0.88}_{-1.14}$	$12.49^{+1.00}_{-1.08}$
$\Lambda_{2.0}$		$36.0^{+47.9}_{-25.1}$	$37.0^{+50.6}_{-26.1}$	$34.7^{+54.0}_{-24.0}$	$33.2^{+30.6}_{-19.1}$	$31.0^{+29.3}_{-17.5}$	$48.9^{+38.6}_{-28.6}$	$44.2^{+43.4}_{-25.4}$
$\rho_{2.0}$	fm^{-3}	$0.615^{+0.381}_{-0.194}$	$0.608^{+0.384}_{-0.194}$	$0.629^{+0.357}_{-0.215}$	$0.636^{+0.273}_{-0.162}$	$0.657^{+0.271}_{-0.168}$	$0.539^{+0.254}_{-0.126}$	$0.572^{+0.263}_{-0.156}$
$P_{2.0}$	MeV/fm^3	$182.14^{+279.85}_{-86.35}$	$178.31^{+280.73}_{-85.35}$	$188.22^{+265.61}_{-95.63}$	$193.66^{+185.95}_{-76.50}$	$204.72^{+190.34}_{-81.94}$	$144.69^{+143.77}_{-51.71}$	$158.67^{+154.34}_{-65.25}$
$\varepsilon_{2.0}$	MeV/fm^3	$677.39^{+544.04}_{-236.40}$	$667.93^{+547.58}_{-235.34}$	$696.14^{+513.13}_{-263.46}$	$704.78^{+385.85}_{-201.48}$	$732.56^{+388.25}_{-212.25}$	$582.67^{+339.60}_{-150.88}$	$624.62^{+359.34}_{-189.97}$
$c_{s,2.0}^2$		$0.573^{+0.087}_{-0.044}$	$0.571^{+0.089}_{-0.044}$	$0.570^{+0.092}_{-0.054}$	$0.577^{+0.057}_{-0.036}$	$0.578^{+0.063}_{-0.046}$	$0.557^{+0.045}_{-0.036}$	$0.552^{+0.054}_{-0.053}$
$\Delta_{2.0}$		$0.065^{+0.052}_{-0.109}$	$0.066^{+0.052}_{-0.111}$	$0.063^{+0.057}_{-0.106}$	$0.059^{+0.042}_{-0.074}$	$0.054^{+0.044}_{-0.075}$	$0.085^{+0.033}_{-0.065}$	$0.080^{+0.039}_{-0.066}$
M_{max}	M_{\odot}	$2.21^{+0.32}_{-0.23}$	$2.22^{+0.33}_{-0.23}$	$2.20^{+0.35}_{-0.21}$	$2.20^{+0.23}_{-0.17}$	$2.18^{+0.22}_{-0.16}$	$2.32^{+0.24}_{-0.24}$	$2.26^{+0.29}_{-0.22}$
$R_{M_{\text{max}}}$	km	$11.05^{+1.18}_{-0.88}$	$11.09^{+1.22}_{-0.91}$	$11.04^{+1.27}_{-0.86}$	$11.44^{+0.88}_{-0.86}$	$10.95^{+0.76}_{-0.53}$	$11.00^{+0.80}_{-0.58}$	$11.32^{+0.97}_{-0.65}$
$\Lambda_{M_{\text{max}}}$		$5.97^{+2.02}_{-1.04}$	$5.95^{+2.02}_{-1.03}$	$6.08^{+2.52}_{-1.10}$	$6.04^{+1.78}_{-0.93}$	$6.19^{+2.19}_{-1.01}$	$5.64^{+2.18}_{-0.73}$	$6.02^{+3.36}_{-1.08}$
$\rho_{M_{\text{max}}}$	fm^{-3}	$0.985^{+0.201}_{-0.205}$	$0.979^{+0.206}_{-0.208}$	$0.994^{+0.189}_{-0.222}$	$0.996^{+0.136}_{-0.152}$	$1.010^{+0.125}_{-0.150}$	$0.912^{+0.169}_{-0.142}$	$0.942^{+0.146}_{-0.169}$
$P_{M_{\text{max}}}$	MeV/fm^3	$583.58^{+100.49}_{-89.44}$	$580.05^{+103.00}_{-90.82}$	$578.91^{+110.00}_{-93.59}$	$588.95^{+62.09}_{-62.70}$	$590.41^{+68.87}_{-61.61}$	$551.63^{+69.28}_{-63.29}$	$551.81^{+71.91}_{-69.80}$
$\varepsilon_{M_{\text{max}}}$	MeV/fm^3	$1284.91^{+263.71}_{-269.12}$	$1276.17^{+270.00}_{-273.02}$	$1295.57^{+250.76}_{-291.27}$	$1298.90^{+177.49}_{-199.98}$	$1317.69^{+165.20}_{-175.72}$	$1189.94^{+219.07}_{-188.08}$	$1227.19^{+188.74}_{-221.17}$
$c_{s,M_{\text{max}}}^2$		$0.728^{+0.039}_{-0.055}$	$0.729^{+0.038}_{-0.055}$	$0.726^{+0.040}_{-0.067}$	$0.726^{+0.032}_{-0.061}$	$0.723^{+0.033}_{-0.061}$	$0.741^{+0.028}_{-0.063}$	$0.730^{+0.038}_{-0.096}$
$\Delta_{M_{\text{max}}}$		$-0.125^{+0.043}_{-0.031}$	$-0.126^{+0.043}_{-0.031}$	$-0.123^{+0.051}_{-0.032}$	$-0.123^{+0.038}_{-0.027}$	$-0.120^{+0.045}_{-0.028}$	$-0.134^{+0.049}_{-0.023}$	$-0.125^{+0.067}_{-0.031}$

[1] G. Raaijmakers, T. E. Riley, A. L. Watts, *et al.*, A *NICER* view of PSR J0030+0451: Implications for the dense matter equation of state, *Astrophys. J. Lett.* **887**, L22 (2019), arXiv:1912.05703 [astro-ph.HE].

[2] P. Landry, R. Essick, and K. Chatziioannou, Nonparametric constraints on neutron star matter with existing and upcoming gravitational wave and pulsar observations, *Phys. Rev. D* **101**, 123007 (2020), arXiv:2003.04880 [astro-ph.HE].

- [3] G. Raaijmakers, S. K. Greif, T. E. Riley, *et al.*, Constraining the dense matter equation of state with joint analysis of NICER and LIGO/Virgo measurements, *Astrophys. J. Lett.* **893**, L21 (2020), arXiv:1912.11031 [astro-ph.HE].
- [4] I. Legred, K. Chatziioannou, R. Essick, S. Han, and P. Landry, Impact of the PSR J0740+6620 radius constraint on the properties of high-density matter, *Phys. Rev. D* **104**, 063003 (2021), arXiv:2106.05313 [astro-ph.HE].
- [5] P. T. H. Pang, I. Tews, M. W. Coughlin, *et al.*, Nuclear Physics Multimessenger Astrophysics Constraints on the Neutron Star Equation of State: Adding NICER’s PSR J0740+6620 Measurement, *Astrophys. J.* **922**, 14 (2021), arXiv:2105.08688 [astro-ph.HE].
- [6] S. Altıparmak, C. Ecker, and L. Rezzolla, On the Sound Speed in Neutron Stars, *Astrophys. J. Lett.* **939**, L34 (2022), arXiv:2203.14974 [astro-ph.HE].
- [7] E. Annala, T. Gorda, E. Katerini, A. Kurkela, J. Nättilä, V. Paschalidis, and A. Vuorinen, Multimessenger Constraints for Ultradense Matter, *Phys. Rev. X* **12**, 011058 (2022), arXiv:2105.05132 [astro-ph.HE].
- [8] E. Annala, T. Gorda, J. Hirvonen, O. Komoltsev, A. Kurkela, J. Nättilä, and A. Vuorinen, Strongly interacting matter exhibits deconfined behavior in massive neutron stars, *Nat. Commun.* **14**, 8451 (2023), arXiv:2303.11356 [astro-ph.HE].
- [9] E. V. Chimenski, R. V. Lobato, A. R. Goncalves, and C. A. Bertulani, Bayesian Exploration of Phenomenological EoS of Neutron/Hybrid Stars with Recent Observations, *Parti.* **6**, 198 (2023), arXiv:2205.01174 [nucl-th].
- [10] N. Rutherford, M. Mendes, I. Svensson, *et al.*, Constraining the Dense Matter Equation of State with New NICER Mass–Radius Measurements and New Chiral Effective Field Theory Inputs, *Astrophys. J. Lett.* **971**, L19 (2024), arXiv:2407.06790 [astro-ph.HE].
- [11] Y.-Z. Fan, M.-Z. Han, J.-L. Jiang, D.-S. Shao, and S.-P. Tang, Maximum gravitational mass $M_{\text{TOV}} = 2.25^{+0.08}_{-0.07} M_{\odot}$ inferred at about 3% precision with multimessenger data of neutron stars, *Phys. Rev. D* **109**, 043052 (2024), arXiv:2309.12644 [astro-ph.HE].
- [12] J. Margueron, R. Hoffmann Casali, and F. Gulminelli, Equation of state for dense nucleonic matter from metamodeling. II. Predictions for neutron star properties, *Phys. Rev. C* **97**, 025806 (2018), arXiv:1708.06895 [nucl-th].
- [13] J. Margueron and F. Gulminelli, Effect of high-order empirical parameters on the nuclear equation of state, *Phys. Rev. C* **99**, 025806 (2019), arXiv:1807.01729 [nucl-th].
- [14] N.-B. Zhang and B.-A. Li, GW190814’s Secondary Component with Mass 2.50–2.67 M_{\odot} as a Superfast Pulsar, *Astrophys. J.* **902**, 38 (2020), arXiv:2007.02513 [astro-ph.HE].
- [15] C. Y. Tsang, M. B. Tsang, W. G. Lynch, R. Kumar, and C. J. Horowitz, Determination of the equation of state from nuclear experiments and neutron star observations, *Nat. Astron.* **8**, 328 (2024), arXiv:2310.11588 [nucl-th].
- [16] C. Mondal and F. Gulminelli, Nucleonic metamodeling in light of multimessenger, PREX-II, and CREX data, *Phys. Rev. C* **107**, 015801 (2023), arXiv:2209.05177 [nucl-th].
- [17] J. Zhou, J. Xu, and P. Papakonstantinou, Bayesian inference of neutron-star observables based on effective nuclear interactions, *Phys. Rev. C* **107**, 055803 (2023), arXiv:2301.07904 [nucl-th].
- [18] M. V. Beznogov and A. R. Raduta, Bayesian Survey of the Dense Matter Equation of State Built upon Skyrme Effective Interactions, *Astrophys. J.* **966**, 216 (2024), arXiv:2308.15351 [astro-ph.HE].
- [19] M. V. Beznogov and A. R. Raduta, Bayesian inference of the dense matter equation of state built upon extended Skyrme interactions, *Phys. Rev. C* **110**, 035805 (2024), arXiv:2403.19325 [nucl-th].
- [20] S. Traversi, P. Char, and G. Pagliara, Bayesian Inference of Dense Matter Equation of State within Relativistic Mean Field Models using Astrophysical Measurements, *Astrophys. J.* **897**, 165 (2020), arXiv:2002.08951 [astro-ph.HE].
- [21] T. Malik, M. Ferreira, B. K. Agrawal, and C. Providência, Relativistic Description of Dense Matter Equation of State and Compatibility with Neutron Star Observables: A Bayesian Approach, *Astrophys. J.* **930**, 17 (2022), arXiv:2201.12552 [nucl-th].
- [22] T. Malik, B. K. Agrawal, and C. Providência, Inferring the nuclear symmetry energy at suprasaturation density from neutrino cooling, *Phys. Rev. C* **106**, L042801 (2022), arXiv:2206.15404 [nucl-th].
- [23] X. Sun, Z. Miao, B. Sun, and A. Li, Astrophysical Implications on Hyperon Couplings and Hyperon Star Properties with Relativistic Equations of States, *Astrophys. J.* **942**, 55 (2023), arXiv:2205.10631 [astro-ph.HE].
- [24] Z. Zhu, A. Li, and T. Liu, A Bayesian Inference of a Relativistic Mean-field Model of Neutron Star Matter from Observations of NICER and GW170817/AT2017gfo, *Astrophys. J.* **943**, 163 (2023), arXiv:2211.02007 [astro-ph.HE].
- [25] M. V. Beznogov and A. R. Raduta, Bayesian inference of the dense matter equation of state built upon covariant density functionals, *Phys. Rev. C* **107**, 045803 (2023), arXiv:2212.07168 [nucl-th].
- [26] T. Malik, M. Ferreira, M. B. Albino, and C. Providência, Spanning the full range of neutron star properties within a microscopic description, *Phys. Rev. D* **107**, 103018 (2023), arXiv:2301.08169 [nucl-th].
- [27] M. Salinas and J. Piekarewicz, Bayesian refinement of covariant energy density functionals, *Phys. Rev. C* **107**, 045802 (2023), arXiv:2301.09692 [nucl-th].
- [28] C. Providência, T. Malik, M. B. Albino, and M. Ferreira, Neutron star equation of state: identifying hadronic matter characteristics, arXiv , 2307.05086 (2023), arXiv:2307.05086 [nucl-th].
- [29] P. Char, C. Mondal, F. Gulminelli, and M. Oertel, Generalized description of neutron star matter with a nucleonic relativistic density functional, *Phys. Rev. D* **108**, 103045 (2023), arXiv:2307.12364 [nucl-th].
- [30] C. Huang, G. Raaijmakers, A. L. Watts, L. Tolos, and C. Providência, Constraining a relativistic mean field model using neutron star mass–radius measurements I: nucleonic models, *Mon. Not. R. Astron. Soc.* **529**, 4650 (2024), arXiv:2303.17518 [astro-ph.HE].
- [31] L. Scurto, H. Pais, and F. Gulminelli, General predictions of neutron star properties using unified relativistic mean-field equations of state, *Phys. Rev. D* **109**, 103015 (2024), arXiv:2402.15548 [nucl-th].
- [32] V. Parmar, V. B. Thapa, A. Kumar, D. Bandyopadhyay, and M. Sinha, Bayesian inference of the dense-matter equation of state of neutron stars with antikaon condensation, *Phys. Rev. C* **110**, 045804 (2024), arXiv:2409.19451 [astro-ph.HE].
- [33] J.-J. Li, Y. Tian, and A. Sedrakian, Bayesian constraints on covariant density functional equations of state of compact stars with new NICER mass-radius measurements, *Phys. Lett. B* **865**, 139501 (2025), arXiv:2412.16513 [hep-ph].
- [34] P. Char and C. Mondal, Exploring the limits of nucleonic metamodeling using different relativistic density functionals, arXiv , 2502.04211 (2025), arXiv:2502.04211 [nucl-th].
- [35] J.-J. Li, Y. Tian, and A. Sedrakian, Bayesian inferences on covariant density functionals from multimessenger astrophys-

- ical data. I. Nucleonic models, arXiv , 2502.20000 (2025), arXiv:2502.20000 [nucl-th].
- [36] D. Vretenar, A. V. Afanasjev, G. A. Lalazissis, and P. Ring, Relativistic Hartree Bogoliubov theory: static and dynamic aspects of exotic nuclear structure, *Phys. Rept.* **409**, 101 (2005).
- [37] T. Niksic, D. Vretenar, and P. Ring, Relativistic Nuclear Energy Density Functionals: Mean-Field and Beyond, *Prog. Part. Nucl. Phys.* **66**, 519 (2011), arXiv:1102.4193 [nucl-th].
- [38] M. Oertel, M. Hempel, T. Klähn, and S. Typel, Equations of state for supernovae and compact stars, *Rev. Mod. Phys.* **89**, 015007 (2017), arXiv:1610.03361 [astro-ph.HE].
- [39] J. Yang and J. Piekarewicz, Covariant Density Functional Theory in Nuclear Physics and Astrophysics, *Ann. Rev. Nucl. Part. Sci.* **70**, 21 (2020), arXiv:1912.11112 [nucl-th].
- [40] A. Sedrakian, J. J. Li, and F. Weber, Heavy baryons in compact stars, *Prog. Part. Nucl. Phys.* **131**, 104041 (2023), arXiv:2212.01086 [nucl-th].
- [41] K. Hebeler, J. M. Lattimer, C. J. Pethick, and A. Schwenk, Equation of state and neutron star properties constrained by nuclear physics and observation, *Astrophys. J.* **773**, 11 (2013), arXiv:1303.4662 [astro-ph.SR].
- [42] J. E. Lynn, I. Tews, J. Carlson, S. Gandolfi, A. Gezerlis, K. E. Schmidt, and A. Schwenk, Chiral Three-Nucleon Interactions in Light Nuclei, Neutron- α Scattering, and Neutron Matter, *Phys. Rev. Lett.* **116**, 062501 (2016), arXiv:1509.03470 [nucl-th].
- [43] C. Drischler, K. Hebeler, and A. Schwenk, Chiral interactions up to next-to-next-to-next-to-leading order and nuclear saturation, *Phys. Rev. Lett.* **122**, 042501 (2019), arXiv:1710.08220 [nucl-th].
- [44] S. Huth, C. Wellenhofer, and A. Schwenk, New equations of state constrained by nuclear physics, observations, and QCD calculations of high-density nuclear matter, *Phys. Rev. C* **103**, 025803 (2021), arXiv:2009.08885 [nucl-th].
- [45] S. Typel and H. H. Wolter, Relativistic mean field calculations with density dependent meson nucleon coupling, *Nucl. Phys. A* **656**, 331 (1999).
- [46] G. A. Lalazissis, T. Niksic, D. Vretenar, and P. Ring, New relativistic mean-field interaction with density-dependent meson-nucleon couplings, *Phys. Rev. C* **71**, 024312 (2005).
- [47] M. Dutra, O. Lourenço, S. S. Avancini, B. V. Carlson, A. Delfino, D. P. Menezes, C. Providência, S. Typel, and J. R. Stone, Relativistic Mean-Field Hadronic Models under Nuclear Matter Constraints, *Phys. Rev. C* **90**, 055203 (2014), arXiv:1405.3633 [nucl-th].
- [48] B. Sun, S. Bhattiprolu, and J. M. Lattimer, Compiled properties of nucleonic matter and nuclear and neutron star models from nonrelativistic and relativistic interactions, *Phys. Rev. C* **109**, 055801 (2024), arXiv:2311.00843 [nucl-th].
- [49] D. H. Youngblood, H. L. Clark, and Y. W. Lui, Incompressibility of Nuclear Matter from the Giant Monopole Resonance, *Phys. Rev. Lett.* **82**, 691 (1999).
- [50] B. G. Todd-Rutel and J. Piekarewicz, Neutron-Rich Nuclei and Neutron Stars: A New Accurately Calibrated Interaction for the Study of Neutron-Rich Matter, *Phys. Rev. Lett.* **95**, 122501 (2005), arXiv:nucl-th/0504034.
- [51] S. Shlomo, V. M. Kolomietz, and G. Colò, Deducing the nuclear-matter incompressibility coefficient from data on isoscalar compression modes, *Eur. Phys. J. A* **30**, 23 (2006).
- [52] A. Le Fèvre, Y. Leifels, W. Reisdorf, J. Aichelin, and C. Hartnack, Constraining the nuclear matter equation of state around twice saturation density, *Nucl. Phys. A* **945**, 112 (2016), arXiv:1501.05246 [nucl-ex].
- [53] P. Danielewicz, R. Lacey, and W. G. Lynch, Determination of the equation of state of dense matter, *Science* **298**, 1592 (2002), arXiv:nucl-th/0208016.
- [54] C. Fuchs, A. Faessler, E. Zabrodin, and Y.-M. Zheng, Probing the nuclear equation of state by K^+ production in heavy ion collisions, *Phys. Rev. Lett.* **86**, 1974 (2001), arXiv:nucl-th/0011102.
- [55] C. Hartnack, H. Oeschler, and J. Aichelin, Hadronic matter is soft, *Phys. Rev. Lett.* **96**, 012302 (2006), arXiv:nucl-th/0506087.
- [56] Y. Wang, C. Guo, Q. Li, A. Le Fèvre, Y. Leifels, and W. Trautmann, Determination of the nuclear incompressibility from the rapidity-dependent elliptic flow in heavy-ion collisions at beam energies 0.4 A–1.0 A GeV, *Phys. Lett. B* **778**, 207 (2018), arXiv:1804.04293 [nucl-th].
- [57] D. Oliinychenko, A. Sorensen, V. Koch, and L. McLerran, Sensitivity of Au+Au collisions to the symmetric nuclear matter equation of state at 2–5 nuclear saturation densities, *Phys. Rev. C* **108**, 034908 (2023), arXiv:2208.11996 [nucl-th].
- [58] P. Russotto, P. Z. Wu, M. Zoric, *et al.*, Symmetry energy from elliptic flow in $^{197}\text{Au}+^{197}\text{Au}$, *Phys. Lett. B* **697**, 471 (2011), arXiv:1101.2361 [nucl-ex].
- [59] P. Russotto, S. Gannon, S. Kupny, *et al.*, Results of the ASY-EOS experiment at GSI: The symmetry energy at suprasaturation density, *Phys. Rev. C* **94**, 034608 (2016), arXiv:1608.04332 [nucl-ex].
- [60] D. Adhikari, H. Albatineh, D. Androic, *et al.* (PREX), Accurate Determination of the Neutron Skin Thickness of ^{208}Pb through Parity-Violation in Electron Scattering, *Phys. Rev. Lett.* **126**, 172502 (2021), arXiv:2102.10767 [nucl-ex].
- [61] D. Adhikari, H. Albatineh, D. Androic, *et al.* (CREX), Precision Determination of the Neutral Weak Form Factor of Ca48, *Phys. Rev. Lett.* **129**, 042501 (2022), arXiv:2205.11593 [nucl-ex].
- [62] B. T. Reed, F. J. Fattoyev, C. J. Horowitz, and J. Piekarewicz, Implications of PREX-2 on the Equation of State of Neutron-Rich Matter, *Phys. Rev. Lett.* **126**, 172503 (2021), arXiv:2101.03193 [nucl-th].
- [63] P.-G. Reinhard, X. Roca-Maza, and W. Nazarewicz, Information Content of the Parity-Violating Asymmetry in Pb208, *Phys. Rev. Lett.* **127**, 232501 (2021), arXiv:2105.15050 [nucl-th].
- [64] R. Essick, P. Landry, A. Schwenk, and I. Tews, Detailed examination of astrophysical constraints on the symmetry energy and the neutron skin of Pb208 with minimal modeling assumptions, *Phys. Rev. C* **104**, 065804 (2021), arXiv:2107.05528 [nucl-th].
- [65] J. Estee, W. G. Lynch, C. Y. Tsang, *et al.* (SPiRiT), Probing the Symmetry Energy with the Spectral Pion Ratio, *Phys. Rev. Lett.* **126**, 162701 (2021), arXiv:2103.06861 [nucl-ex].
- [66] J. Margueron, R. Hoffmann Casali, and F. Gulminelli, Equation of state for dense nucleonic matter from metamodelling. I. Foundational aspects, *Phys. Rev. C* **97**, 025805 (2018), arXiv:1708.06894 [nucl-th].
- [67] J. J. Li and A. Sedrakian, Constraining compact star properties with nuclear saturation parameters, *Phys. Rev. C* **100**, 015809 (2019), arXiv:1903.06057 [astro-ph.HE].
- [68] J. J. Li and A. Sedrakian, Implications from GW170817 for Δ -isobar Admixed Hypernuclear Compact Stars, *Astrophys. J. Lett.* **874**, L22 (2019), arXiv:1904.02006 [nucl-th].
- [69] J. J. Li and A. Sedrakian, New Covariant Density Functionals of Nuclear Matter for Compact Star Simulations, *Astrophys. J.* **957**, 41 (2023), arXiv:2308.14457 [nucl-th].
- [70] S. Huth, P. T. H. Pang, I. Tews, *et al.*, Constraining Neutron-Star Matter with Microscopic and Macroscopic Collisions, *Nature* **606**, 276 (2022), arXiv:2107.06229 [nucl-th].

- [71] J. Antoniadis, P. C. C. Freire, N. Wex, *et al.*, A Massive Pulsar in a Compact Relativistic Binary, *Science* **340**, 6131 (2013), [arXiv:1304.6875 \[astro-ph.HE\]](#).
- [72] B. P. Abbott, R. Abbott, T. D. Abbott, *et al.* (LIGO Scientific, Virgo), GW170817: Observation of Gravitational Waves from a Binary Neutron Star Inspiral, *Phys. Rev. Lett.* **119**, 161101 (2017), [arXiv:1710.05832 \[gr-qc\]](#).
- [73] B. P. Abbott, R. Abbott, T. D. Abbot, *et al.* (LIGO Scientific, Virgo), Properties of the binary neutron star merger GW170817, *Phys. Rev. X* **9**, 011001 (2019), [arXiv:1805.11579 \[gr-qc\]](#).
- [74] B. P. Abbott, R. Abbott, T. D. Abbott, *et al.* (LIGO Scientific, Virgo), GW190425: Observation of a Compact Binary Coalescence with Total Mass $\sim 3.4M_{\odot}$, *Astrophys. J. Lett.* **892**, L3 (2020), [arXiv:2001.01761 \[astro-ph.HE\]](#).
- [75] F. Hernandez Vivanco, R. Smith, E. Thrane, and P. D. Lasky, A scalable random forest regressor for combining neutron-star equation of state measurements: A case study with GW170817 and GW190425, *Mon. Not. R. Astron. Soc.* **499**, 5972 (2020), [arXiv:2008.05627 \[astro-ph.HE\]](#).
- [76] T. Salmi, D. Choudhury, Y. Kini, *et al.*, The Radius of the High-mass Pulsar PSR J0740+6620 with 3.6 yr of NICER Data, *Astrophys. J.* **974**, 294 (2024), [arXiv:2406.14466 \[astro-ph.HE\]](#).
- [77] S. Vinciguerra, T. Salmi, A. L. Watts, *et al.*, An Updated Mass–Radius Analysis of the 2017–2018 NICER Data Set of PSR J0030+0451, *Astrophys. J.* **961**, 62 (2024), [arXiv:2308.09469 \[astro-ph.HE\]](#).
- [78] D. Choudhury, T. Salmi, S. Vinciguerra, *et al.*, A NICER View of the Nearest and Brightest Millisecond Pulsar: PSR J0437–4715, *Astrophys. J. Lett.* **971**, L20 (2024), [arXiv:2407.06789 \[astro-ph.HE\]](#).
- [79] T. Salmi, J. S. Deneva, P. S. Ray, *et al.*, A NICER View of PSR J1231–1411: A Complex Case, *Astrophys. J.* **976**, 58 (2024), [arXiv:2409.14923 \[astro-ph.HE\]](#).
- [80] T. E. Riley, A. L. Watts, S. Bogdanov, *et al.*, A NICER View of PSR J0030+0451: Millisecond Pulsar Parameter Estimation, *Astrophys. J. Lett.* **887**, L21 (2019), [arXiv:1912.05702 \[astro-ph.HE\]](#).
- [81] T. E. Riley, A. L. Watts, P. S. Ray, *et al.*, A NICER View of the Massive Pulsar PSR J0740+6620 Informed by Radio Timing and XMM-Newton Spectroscopy, *Astrophys. J. Lett.* **918**, L27 (2021), [arXiv:2105.06980 \[astro-ph.HE\]](#).
- [82] M. C. Miller, F. K. Lamb, A. J. Dittmann, *et al.*, PSR J0030+0451 Mass and Radius from NICER Data and Implications for the Properties of Neutron Star Matter, *Astrophys. J. Lett.* **887**, L24 (2019), [arXiv:1912.05705 \[astro-ph.HE\]](#).
- [83] M. C. Miller, F. K. Lamb, A. J. Dittmann, *et al.*, The Radius of PSR J0740+6620 from NICER and XMM-Newton Data, *Astrophys. J. Lett.* **918**, L28 (2021), [arXiv:2105.06979 \[astro-ph.HE\]](#).
- [84] R. Abbott, T. D. Abbott, S. Abraham, *et al.* (LIGO Scientific, Virgo), GW190814: Gravitational Waves from the Coalescence of a 23 Solar Mass Black Hole with a 2.6 Solar Mass Compact Object, *Astrophys. J. Lett.* **896**, L44 (2020), [arXiv:2006.12611 \[astro-ph.HE\]](#).
- [85] Y. Fujimoto, K. Fukushima, L. D. McLerran, and M. Praszalowicz, Trace Anomaly as Signature of Conformality in Neutron Stars, *Phys. Rev. Lett.* **129**, 252702 (2022), [arXiv:2207.06753 \[nucl-th\]](#).
- [86] D. Klahn, T. Blaschke, S. Typel, *et al.*, Constraints on the high-density nuclear equation of state from the phenomenology of compact stars and heavy-ion collisions, *Phys. Rev. C* **74**, 035802 (2006), [arXiv:nucl-th/0602038](#).
- [87] J. Boguta, Density Dependence of the Single Particle Potential in Nuclear Matter, *Phys. Lett. B* **106**, 250 (1981).
- [88] J. Boguta and H. Stocker, Systematics of nuclear matter properties in a non-linear relativistic field theory, *Phys. Lett. B* **120**, 289 (1983).